



ARL-TR-8962 • MAY 2020



Micro-CT-Based Three-Layer Finite Element Model for Quasi-Static Human Skull Indentation

by Stephen L Alexander, P Justin McKee, and
Tusit Weerasooriya

Approved for public release; distribution is unlimited.

NOTICES

Disclaimers

The research reported in this document was performed in connection with contract/instrument W911QX-16-D-0014 with the US Army Research Laboratory. (As of 31 January 2019, the organization is now part of the US Army Combat Capabilities Development Command [formerly RDECOM] and is now called CCDC Army Research Laboratory.)

The views and conclusions contained in this document are those of SURVICE Engineering Company and the CCDC Army Research Laboratory. Citation of manufacturer's or trade names does not constitute an official endorsement or approval of the use thereof. The US Government is authorized to reproduce and distribute reprints for Government purposes notwithstanding any copyright notation hereon.

The findings in this report are not to be construed as an official Department of the Army position unless so designated by other authorized documents.

Destroy this report when it is no longer needed. Do not return it to the originator.



Micro-CT-Based Three-Layer Finite Element Model for Quasi-Static Human Skull Impact

Stephen L Alexander
SURVICE Engineering Company

P Justin McKee and Tusit Weerasooriya
Weapons and Materials Research Directorate, CCDC Army Research Laboratory

REPORT DOCUMENTATION PAGE

*Form Approved
OMB No. 0704-0188*

Public reporting burden for this collection of information is estimated to average 1 hour per response, including the time for reviewing instructions, searching existing data sources, gathering and maintaining the data needed, and completing and reviewing the collection information. Send comments regarding this burden estimate or any other aspect of this collection of information, including suggestions for reducing the burden, to Department of Defense, Washington Headquarters Services, Directorate for Information Operations and Reports (0704-0188), 1215 Jefferson Davis Highway, Suite 1204, Arlington, VA 22202-4302. Respondents should be aware that notwithstanding any other provision of law, no person shall be subject to any penalty for failing to comply with a collection of information if it does not display a currently valid OMB control number.

PLEASE DO NOT RETURN YOUR FORM TO THE ABOVE ADDRESS.

1. REPORT DATE (DD-MM-YYYY) May 2020		2. REPORT TYPE Technical Report		3. DATES COVERED (From - To) 01 January 2018–30 September 2019	
4. TITLE AND SUBTITLE Micro-CT-Based Three-Layer Finite Element Model for Quasi-Static Human Skull Impact				5a. CONTRACT NUMBER W911QX-16-D-0014	
				5b. GRANT NUMBER	
				5c. PROGRAM ELEMENT NUMBER	
6. AUTHOR(S) Stephen L Alexander, P Justin McKee, and Tusit Weerasooriya				5d. PROJECT NUMBER	
				5e. TASK NUMBER	
				5f. WORK UNIT NUMBER	
7. PERFORMING ORGANIZATION NAME(S) AND ADDRESS(ES) CCDC Army Research Laboratory ATTN: FCDD-RLW-PB Aberdeen Proving Ground, MD 21005				8. PERFORMING ORGANIZATION REPORT NUMBER ARL-TR-8962	
9. SPONSORING/MONITORING AGENCY NAME(S) AND ADDRESS(ES)				10. SPONSOR/MONITOR'S ACRONYM(S)	
				11. SPONSOR/MONITOR'S REPORT NUMBER(S)	
12. DISTRIBUTION/AVAILABILITY STATEMENT Approved for public release; distribution is unlimited.					
13. SUPPLEMENTARY NOTES ORCID ID: Tusit Weerasooriya, 0000-0003-3299-2166					
14. ABSTRACT Recently, quasi-static indentation experiments on human skull specimens were uniquely designed and performed at the US Army Combat Capabilities Development Command Army Research Laboratory to study the deformation and failure responses and associated mechanisms. The fully instrumented experiments involved skullcap specimens which included more of the 3-D curvature of the skull than coupon-level studies, thereby the multi-axial stress state that governs the impact response more closely represented <i>in vivo</i> loading conditions. Here, one of the indentation experiments on a human parietal skullcap was modeled using finite element simulation, with a simplified concept specifically developed to ease transition of the methodology into larger-scale simulations involving the whole head. The region of the skullcap near the point of loading included the full thickness of the skull, with both the outer and inner surfaces intact. This central region was modeled as a composite of three layers: the outer table, mid-diploe, and inner table. The relative thickness of each of the layers was specified to match the thickness measurements previously reported using a quantitative method for identification of layer boundaries. In the regions away from the point of loading, the skullcap was modeled as a single, composite homogeneous layer. The mechanical properties for each of the three layers, as well as for the composite region, were set to previously reported moduli, using specifically parietal bone data. The evolution of the contact load and backface deformation of the simulation matched the experimental measurements within 4% and 24%, respectively, thus demonstrating the ability of the previously reported values for geometry and moduli to model the initial linear deformation response of the skull. Furthermore, the improved accuracy of the heterogeneous method for material property assignment was demonstrated by comparing these measurements with a simulation using only the composite properties.					
15. SUBJECT TERMS human skull simulation; human skull mechanical properties; human skull compression; finite element simulation; material mapping					
16. SECURITY CLASSIFICATION OF:			17. LIMITATION OF ABSTRACT UU	18. NUMBER OF PAGES 41	19a. NAME OF RESPONSIBLE PERSON Stephen L Alexander
a. REPORT Unclassified	b. ABSTRACT Unclassified	c. THIS PAGE Unclassified			19b. TELEPHONE NUMBER (Include area code) (410) 306-0917

Standard Form 298 (Rev. 8/98)
Prescribed by ANSI Std. Z39.18

Contents

List of Figures	v
List of Tables	vi
Acknowledgments	vii
1. Introduction	1
2. Methods	3
2.1 Specimen Extraction	3
2.2 Experiment	4
2.3 Skullcap Mesh Generation and Element Material Assignment	5
2.3.1 Creating the Image-Sets for the Scoring Matrix	7
2.3.2 Assembling the Scoring Matrix in MATLAB	9
2.3.3 Comparing Element Location with the Scoring Matrix	10
2.3.4 Material Properties	11
2.4 Finite Element Simulation Setup and Execution	12
2.4.1 Indenter	13
2.4.2 Backing Plate	14
2.4.3 Contact	15
3. Results	15
3.1 Indenter Load-Displacement	15
3.2 Backface Displacement	16
3.2.1 Maximum Backface Displacement and Plate Displacement	17
3.2.2 Relative BD Profile	18
4. Discussion	19
5. Conclusion and Future Work	21
6. References	22

Appendix A. Contours of Fullfield Backface Displacement	24
Appendix B. Effect of the Friction Coefficient between Skullcap and Backing Plate	26
List of Symbols, Abbreviations, and Acronyms	29
Distribution List	30

List of Figures

Fig. 1	Skullcap specimen next to the skull from which it was extracted (Panel A), and reannotated (Panel B) to indicate the point of contact with the indenter (center of crosshairs). Scale-bar of Panel B is in inches. The following aspects of the skullcap are labeled: anterior (A, toward the front of the head), posterior (P, toward the rear), superior (S, toward the top of the head), and inferior (I, toward the shoulders).	4
Fig. 2	A cross-sectional image from the micro-CT scan. The superior and inferior regions of the skullcap are identified. The 3-layer region (3LR) is identified as the central region, where both the outer and inner skull surfaces are present. The composite regions are toward the periphery.	5
Fig. 3	Creating the image-sets that were subsequently output to the MATLAB database (Scoring Matrix) for element material assignment. Steps A-H are described in Section 2.3.1. Boxes with a green background represent steps that were executed within the CTAn software (Bruker micro-CT.) Step C was executed within MATLAB, and Step E was completed within Inkscape.	6
Fig. 4	Thickness percentage of the three layers: outer table, diploe, and inner table, (reproduced from Alexander et al. 2019). The results are separated between frontal and parietal bones.	8
Fig. 5	Creation of the MATLAB Scoring Matrix. Four image-sets from the process outlined in Fig. 3 were loaded into MATLAB and added together. The resulting dataset contained values, which ranged from 0 to 4, as described in Table 1.	10
Fig. 6	Volumetric mesh showing the assignment of the different materials.	11
Fig. 7	Steps taken from the micro-CT image-set to the execution of the finite element simulation.	13
Fig. 8	Skullcap and indenter, viewed from above (left) and from an anterior-posterior cross section (right). The colors within the skullcap mesh indicate the materials of the elements and correspond with those used in Fig. 6.	14
Fig. 9	Assembly of the aluminum backing plate, specimen, and indenter. Four of the nodes used to constrain the plate in the x-z plane are circled in red.	14
Fig. 10	Load-displacement curve for the indenter, measured during the experiment and simulation. The linear portion of the experimental load-displacement curve is highlighted (black dashed line), and is also replotted from the origin (solid black line). Four timepoints in the simulation that are used for comparison between the simulation and experiment (Section 3.2) are noted by t08-t11.	16

Fig. 11	Contours of the BD for the backface of the skullcap and the plate at the timepoint t11 (timepoints were defined in Fig. 10). The contours from the experiment and simulation are shown on the left and right, respectively. The plate is identified in the simulation by the larger elements, the skullcap by the much smaller elements. Similar contours for t08–t10 are included in Appendix A. 17
Fig. 12	The maximum BD of the skullcap (BD_{max}), and the BD at several points around the perimeter of the hole in the backing plate (Plate Points of Extraction), are plotted as a function of the displacement applied by the indenter. The location of BD_{max} and the Plate Points of Extraction are shown in Fig. 11. 18
Fig. 13	Relative BD profiles of the skullcap zeroed to the plate for the timepoints t08–t11 (timepoints were defined in Fig. 10). The relative BD is plotted for points along the Lines of Extraction (location shown in Fig. 11). The BD profile is plotted as a function of distance in the z-dimension (Fig. 11) from the point of BD_{max} . The location of BD_{max} was under the POI and is marked as “X” in Fig. 11. 19
Fig. 14	Relative BD profile at t11 and indentation load when all elements are assigned the same composite mechanical properties (green line). (Left) The BD profile at timepoint t11, relative to the plate. (Right) The load-displacement curves compared to the linear regime of the experiment, which was identified in Fig. 10. 20
Fig. A-1	Full-field BD contours from the experiment (left column) and simulation (right column) for the timepoints t08–11. The timepoints were previously defined in Fig. 10 of the main report, which is reproduced on the right. 25
Fig. B-1	Load-displacement response of the heterogeneous simulation using different values of the frictional coefficient between the skullcap and the backing plate. The case of $\mu = 0.5$ (blue curve) corresponds to the heterogeneous simulation presented in Section 3. 27

List of Tables

Table 1	Physical meaning of the Scoring Matrix values 10
Table 2	The material properties of the four different element materials. Elastic moduli were taken from the results of ARL-TR-8512 (Alexander et al. 2018). The bone volume fractions were taken from the results of Alexander et al. 2019. 12
Table 3	Relative BD_{max} at timepoint t11 and the skullcap stiffness. The experimental stiffness is from the linear regime, which was identified in Fig. 10. 20
Table B-1	Skullcap stiffness 28

Acknowledgments

The authors would like to acknowledge the contributions of the following US Army Combat Capabilities Development Command Army Research Laboratory researchers: Timothy Walter for performing the micro-CT scans of the skullcap specimen and Carolyn Hampton for assistance with the Hypermesh software and using the High Performance Computing systems. We would also like to acknowledge Amy Dagro for suggesting how to proceed in modeling contact in Abaqus.

1. Introduction

Due to the prevalence of brain injury in the battlefield, a number of ongoing research programs are aimed at quantifying the response of the human head to applied loading. Many of these programs have a component involved with finite element simulations. While the simulations provide additional insight into the experimental result, the computational capabilities especially enable researchers to investigate scenarios and parameter space that would not be feasible experimentally.

Finite element analysis (FEA) relies upon accurate mathematical representation of materials response (material model or deformation and failure models) of the subcomponents of the systems. As the natural protector of the brain, the skull is a key component for research into head protection and brain injury. The human skull is a sandwich structure comprising three layers based on porosity distribution in the through-thickness direction: the outer table (nearest to the skin), the mid-diploe, and the inner table (nearest to the brain). Generally, the outer table and inner table can be characterized as consisting of denser, cortical bone, while the diploe is made of more porous, trabecular bone. This sandwich structure can be expected to cause the skull to have a significant gradient in mechanical properties from the inner to outer surfaces, since the mechanical properties of bone are known to vary significantly (power-law) with bone volume fraction (Morgan et al. 2003, Helgason et al. 2008). Therefore, modeling (mathematically representing) this heterogeneity would aid the biofidelity of human head simulations. Indeed, explicit modeling of the heterogeneous properties of skull bone has been demonstrated to have a significant impact on the results of whole head simulations. For example, the Gottingen minipig cranium demonstrated microstructural variation between the inner surface and outer surface (Alexander et al. 2016). Therefore, in simulating impact to the minipig head, Thompson et al. (2016) compared a mesh assigned homogenous skull properties to a mesh that divided the thickness of the skull, between the inner and outer surface, as 10 different layers near the impact point. Experimentally derived mechanical properties were assigned to each of the 10 layers, and including these heterogeneous, biofidelic mechanical properties significantly changed the predictions of peak pressure measured within the brain.

One class of methods used to model material heterogeneity assigns unique material properties to elements based on the average density in the volume of the physical bone represented by the element. These methods map the spatial location of the element within the finite element mesh to the physical area of a high-resolution image set, such as micro-computed tomography (micro-CT). Algorithms for mapping the elements to the images have been implemented in several commercial

software programs (e.g., Mimics and Simpleware) and researcher-developed routines (e.g., Bessho et al. 2007, Chen et al. 2010). Using such a method to calculate the density of each element, a researcher is then able to apply a relationship between the modulus and the density in order to assign unique, microstructurally-derived moduli to each element. The literature contains many examples of linear and power relations between the modulus and the density of bone (reviewed by Helgason et al. 2008). This methodology has been successfully demonstrated in accurate, biofidelic modeling of organ-level experiments, such as femur (Dall'Ara et al. 2013) and vertebrae (Brown et al. 2014).

Similarly, a power law relationship between the bone volume fraction and the modulus was recently obtained with critical assumptions, and published specifically for the human skull (Alexander et al. 2018, 2020a). This power law relationship was then implemented in a 3-D finite element simulation of quasi-static compression, which used a coarse-grained mesh and assigned elastic moduli to elements based on their bone volume fraction, thereby representing the 3-D heterogeneous microstructure (Alexander et al. 2020b). The simulation, without the assumptions that were used to obtain the power law from experiments, closely represented the load-displacement and surface strain field response, thereby demonstrating the utility of the power law relationship and the used meshing concept.

In addition to the element-by-element concept, different sets of elastic moduli for the human skull were calculated from the power law relationship to be used in simulations at various levels of mesh complexity (Tables 3 and 4 of Alexander et al. 2020a). These various sets of moduli were reported since many simulations are at a much larger length scale than an individual bone, such as the entire head (Zhang et al. 2018) or body (Dagro et al. 2013). The larger numbers of elements in larger-scale simulations would make the assignment of material properties to individual elements not practical. A simpler approach to increasing biofidelity of larger-scale simulations involving the head would be to explicitly model the three layers of the sandwich structure: the outer table, mid-diploe, and inner table. Then each layer would be assigned appropriate meso-scale mechanical properties, analogous to the work of Thompson et al. (2016) in meshing the minipig skull in the region of impact as a series of layers from the inner to outer surface.

In this paper, the three layers of the human skull are meshed based on a previously reported layer thicknesses study (Alexander et al. 2019) and layer moduli study (Alexander et al. 2020a). The ability of this meshing technique, informed by the thicknesses and moduli of the previous reports, to accurately simulate a quasi-static indentation experiment performed on a slice of skull bone (skullcap) is evaluated. The uniquely developed experiment enabled accurate measurement of the backface

deformation of the skull in response to indentation. Backface deformation, a key factor for assessing the possibility of brain injury, is used as a metric for comparison between the simulation and the experiment. Here, the details of the experiment are first briefed. The method used for determining the layer-region of each element, based on its spatial location, is then presented. Boundary conditions and loading conditions used in the simulation are then detailed. Finally, the resulting indentation contact force and backface deformation are compared to the corresponding experimental results.

2. Methods

2.1 Specimen Extraction

The experiments documented here were conducted in compliance with the US Army Combat Capabilities Development Command (CCDC) Army Research Laboratory's (ARL's) Policy for Use of Human Cadavers for Research, Development, Test, and Evaluation under the guidance and oversight of the CCDC Army Research Laboratory Human Cadaver Review Board and the ARL Safety Office. One human skullcap specimen was extracted from the left parietal bone of a single post-mortem human subject using a pathology bone saw (EXAKT 312, EXAKT Technologies, Inc.). The donor for this specimen was a 78-year-old male with a body mass of 66 kg at death. Care was taken to ensure that the specimen did not cross any suture lines. After extraction, the specimen was wet-sanded by hand to ensure flatness. Figure 1 shows the skullcap specimen. The different physical sides of the specimen will be referred to in this report with the following terms: anterior (towards the front of the head), posterior (towards the rear of the head), superior (towards the top of the head), and inferior (towards the shoulders.) The dimension spanning the thickness from the inner surface (nearest the brain) to the outer surface (nearest the skin) will be referred to as the through-thickness dimension.

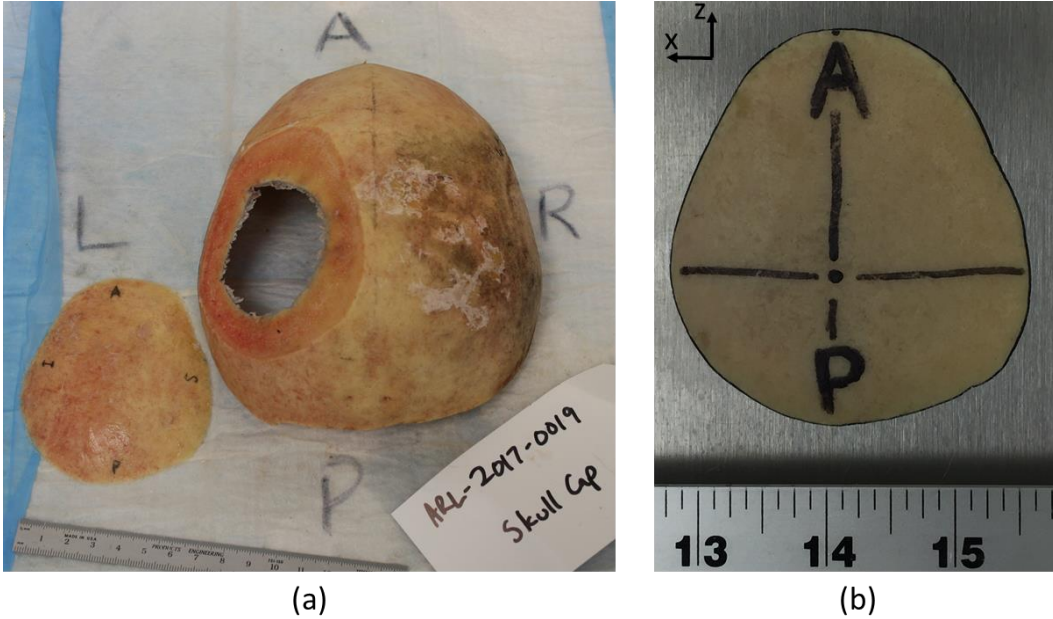


Fig. 1 Skullcap specimen next to the skull from which it was extracted (Panel A), and reannotated (Panel B) to indicate the point of contact with the indenter (center of crosshairs). Scale-bar of Panel B is in inches. The following aspects of the skullcap are labeled: anterior (A, toward the front of the head), posterior (P, toward the rear), superior (S, toward the top of the head), and inferior (I, toward the shoulders).

2.2 Experiment

This experiment is part of a larger study on the mechanical response of human skull to indentation loading (Gunnarsson et al. 2019) and is described here for completeness. The microstructure of the specimen was characterized using high-resolution CT (Northstar XRD 1620) with an isotropic voxel size of $24.4 \mu\text{m}$. After scanning, the skullcap was loaded using an indentation technique at a quasi-static rate. This indentation was generated via load frame (Instron 8871) with a steel indenter tip attached to the crosshead. The point of contact between the indenter and the specimen (Point of Impact [POI]) was at approximately the highest point of the skullcap, as shown in Fig. 1b. The specimen was approximately 5.9 mm thick under this impact point, as measured from the micro-CT images. The indenter moved into the specimen, in the through-thickness direction, at a constant rate of 0.005 mm/s. The specimen was supported by a lubricated aluminum backing plate and rested freely on the plate, unconstrained in the plane surface of the plate. The plane of the plate will hereafter be referred to as the orthogonal plane, as it was perpendicular to the direction of indentation. The coordinate system was defined such that indenter motion was in the y-dimension (Fig. 2) and the orthogonal plane was the x-z plane (Fig. 1b). The backing plate had a hole at the center. Through this hole, cameras were used to observe and record the deformation history of the skull

inner surface during indentation. The plate opening was fabricated by first tracing the perimeter of the skullcap on the plate, and then moving this trace towards the center of the plate by 0.25 inch.

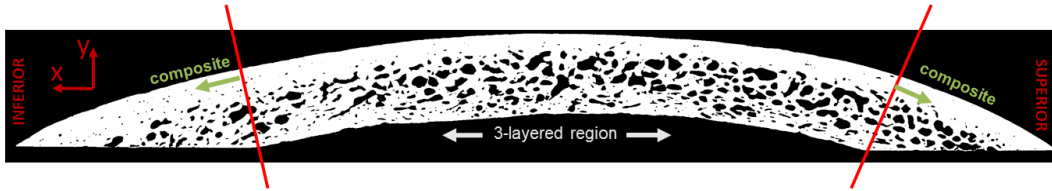


Fig. 2 A cross-sectional image from the micro-CT scan. The superior and inferior regions of the skullcap are identified. The 3-layer region (3LR) is identified as the central region, where both the outer and inner skull surfaces are present. The composite regions are toward the periphery.

Both the back surface of the skullcap, as well as the bottom of the aluminum plate, were speckled to track displacement using digital image correlation (DIC). Two framing cameras (Point Grey Research, 12.3 MP) captured images of the specimen and plate at 1 frame per second (fps). These images were later postprocessed to measure the out-of-plane deformation and the strain field on the skull specimen inner surface, and also of the bottom of the plate during deformation (Vic-3D, Correlated Solutions). Load on the skull specimen was measured using a traditional load cell (Instron capacity 5 kN). After loading, the skull specimens were CT-scanned to obtain quantitative data on fracture and damage caused to the structure, with the pretest and posttest images coregistered using DataViewer software (Bruker microCT).

2.3 Skullcap Mesh Generation and Element Material Assignment

The micro-CT images were first binarized using the Otsu algorithm (Otsu 1975). The skullcap specimen was separated into two regions, as shown in Fig. 2. A central region was identified in which the entire thickness of the skull was preserved including both the outer and inner tables, and will be referred to as the 3-layer region (3LR). The three layers were represented in the model and defined with unique material properties. However, not all three layers were preserved away from the center of the specimen, in the area where the skullcap had been cut flat to rest on the backing plate. This peripheral region will be referred to as the “composite” region, and was modeled as a single homogenized material.

For mesh generation, the images were subsequently resized by a factor of 3: the original resolution of the images (24.4 μm , Section 2.2) was reduced to a final resolution of 73.2 μm (Fig. 3a). The resolution was lowered to smooth the data to ease the process of surface generation. Otherwise, if the original image resolution

was used, the resulting surface meshes would have been unnecessarily large in size and intractable, since the software would have tried to capture the finer details in the high-resolution images. Resizing improved surface generation by removing the finer features, which would have later been lost in the mesh generation process. The images were loaded into CTAn software (Bruker microCT), where a shrink-wrapped region of interest (ROI) was created for each image (Fig. 3b). The shrinkwrapped ROI represented the outer bounds of the specimen, with all internal pores and geometry completely filled. A stereolithography (STL) file of the shrinkwrapped ROI was then created in the CTAn software using a smoothing algorithm proprietary to the software (Adaptive Rendering). The nodal coordinates of the STL file were saved in units of voxels.

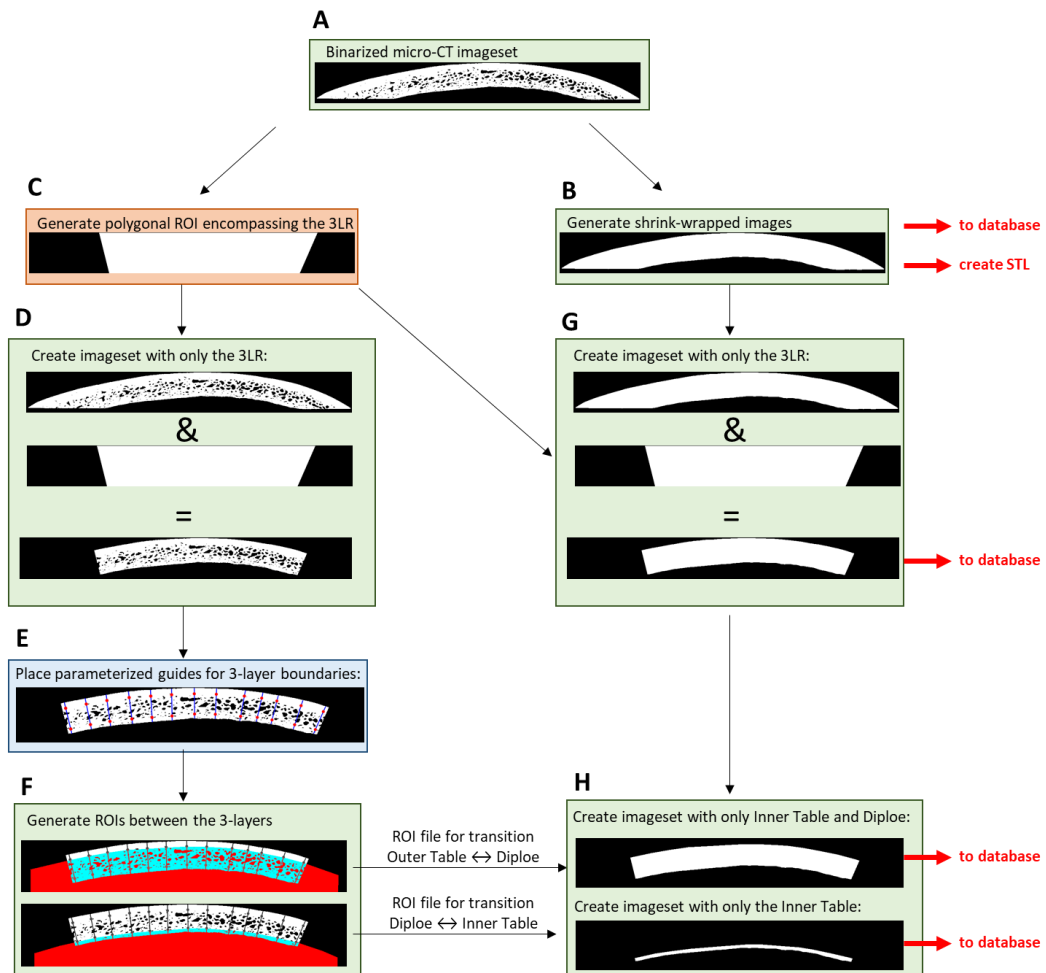


Fig. 3 Creating the image-sets that were subsequently output to the MATLAB database (Scoring Matrix) for element material assignment. Steps A-H are described in Section 2.3.1. Boxes with a green background represent steps that were executed within the CTAn software (Bruker micro-CT.) Step C was executed within MATLAB, and Step E was completed within Inkscape.

The STL was imported into Ansys ICEM as faceted geometry. The STL was further smoothed with the shrinkwrap function within ICEM. Next, the bottom surface of the specimen was flattened. In Blender, nodes with the least y-coordinate value were identified. All nodes within 2° of the identified nodes were constrained to the same y-coordinate. The smoothed STL file was then loaded into the Hypermesh software, where tetrahedral meshing was performed with a target element size of 11 voxels (0.8 mm), creating 451,070 elements.

Elements were assigned one of these four different materials: outer table, diploe, inner table, or composite. Material assignment was based on the spatial location of the element within the mesh. Specifically, the coordinates of the element were compared with an image database created in MATLAB, hereafter referred to as the “Scoring Matrix”. The Scoring Matrix was constructed such that locations corresponding to each of the four different materials were given a unique value. The locations of each material were identified by importing four different image-sets: showing the entire specimen, the 3LR, only the inner table together with the diploe, and one showing only the inner table. The process used to create these images is shown schematically in Fig. 3. The letter markings of Fig. 3 correspond with Steps A through H.

2.3.1 Creating the Image-Sets for the Scoring Matrix

2.3.1.1 Steps A and B: Resizing the image-set; creating the “filled-in” image-set

The micro-CT images were first resized (Step A). The resized images were then loaded into CTAn. Then, the image-set corresponding to the “filled-in” geometry was created with the shrink-wrap operation (Step B). The STL was created from the shrink-wrapped image-set.

2.3.1.2 Step C: Identification of the boundary between the 3LR and the Composite Region

First, the boundary between the 3LR and Composite Region was identified. The cross-sectional images were loaded into MATLAB. The 3LR was identified as those areas of the image for which a vector drawn normal to the outer surface would pass through the inner table. The determination was done by visual inspection of the image within MATLAB. A polygonal ROI was then manually created within MATLAB (*roipoly* function), which encompassed the 3LR of the image. This process was repeated for nine different images (cross-sectional slices of the volume). A routine was written in MATLAB to interpolate between the nine user-defined polygonal ROIs, in order to create an ROI for each of the remaining cross-

sectional images. A new image set was created that contained only these polygonal ROIs (Fig. 3c).

2.3.1.3 Step D: Creation of the image-set containing only the 3LR

The polygonal ROI image-set from Step C was then loaded into the CTAn software together with the original dataset. The logical, bitwise AND operation between the original images and the polygonal ROI images was used to generate the image-set containing only the 3LR (Fig. 3d).

2.3.1.4 Step E: Identification of the boundaries between the outer table, diploe, and inner table

Next, the boundaries between the three layers (outer table, diploe, and inner table) were quantitatively identified. The boundaries were taken from the results of Alexander et al. (2019), which reported the thickness percentage of the outer table, diploe, and inner table for parietal bones to be 19%, 66%, and 15%, respectively (reproduced in Fig. 4). The nine cross-sectional images, which were used to specify the polygonal ROI (from Step C), were loaded into Inkscape. A guide was created within Inkscape with demarcations at 19% and 85% of the length to represent the transitions between the outer table to diploe (at 19%) and diploe to inner table (19%+66%=85%). Within Inkscape, these guides were proportionately scaled and overlaid on the images, in an alignment roughly normal with the outer surface. An example of an image with these overlaid guides is shown in Fig. 3e.

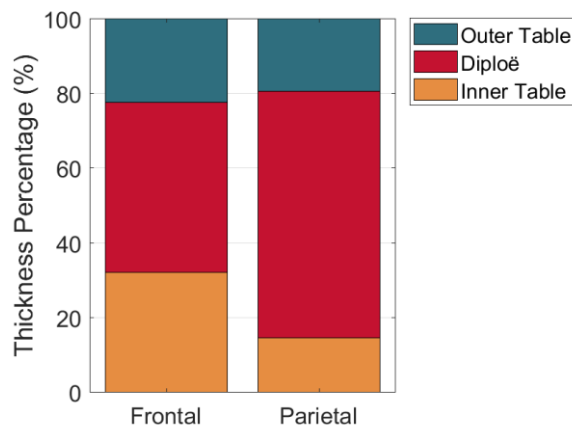


Fig. 4 Thickness percentage of the three layers: outer table, diploe, and inner table, (reproduced from Alexander et al. 2019). The results are separated between frontal and parietal bones.

2.3.1.5 Step F: Creation of ROI files for the transitions between the three layers
The annotated images from Step E were loaded into CTAn together with the 3LR image-set. Polygonal ROIs were created on the nine annotated images from Step E, by connecting the demarcations. Two separate polygonal ROIs were created: one that indicated the transition between the outer table and diploe, and another for the transition between the diploe and inner table. After the polygons were specified on the nine annotated images, the CTAn software interpolated the ROIs to the remaining cross-sectional images. The two ROIs were individually saved as CTAn .roi files.

2.3.1.6 Step G

The 3LR of the shrinkwrapped image-set was saved as a unique image-set by following an analogous procedure to Step D. The polygonal ROI identifying the boundary between the 3LR and Composite Region (created in Step C) was loaded into CTAn together with the shrinkwrapped image-set, and the logical AND operation was applied.

2.3.1.7 Step H

The image-set generated by Step G was loaded into CTAn, and the .roi files generated by Step F were applied. The logical AND operation between the images and the ROI indicating the transition between the outer table and diploe was used to create an image-set that contained only the inner table and diploe within the 3LR. Similarly, the logical AND operation between the images and the ROI indicating the transition between the diploe and the inner table was used to create an image-set that contained only the inner table within the 3LR.

2.3.2 Assembling the Scoring Matrix in MATLAB

First, the shrinkwrapped images corresponding to the whole specimen (from Step B) were loaded into MATLAB as a logical matrix (*imread* function). Therefore, each pixel within the specimen (appearing as white in the image) was represented by 1, while each pixel outside of the specimen (appearing as black in the image) was represented by 0. Similarly, a logical matrix was created from reading the shrinkwrapped image-set containing only the 3LR (Step G). Finally, the image-set containing the inner table and diploe and the image-set containing only the diploe (from Step H) were also loaded into MATLAB and saved as separate logical matrices.

Four logical matrices had been created by this process, corresponding to the complete skullcap, the complete 3LR, the inner table combined with the diploe, and the inner table alone. These four matrices were then summed together to create the

Scoring Matrix (Fig. 5). As a result of the summation, the values within the Scoring Matrix ranged from 0 to 4, as shown in Table 1.

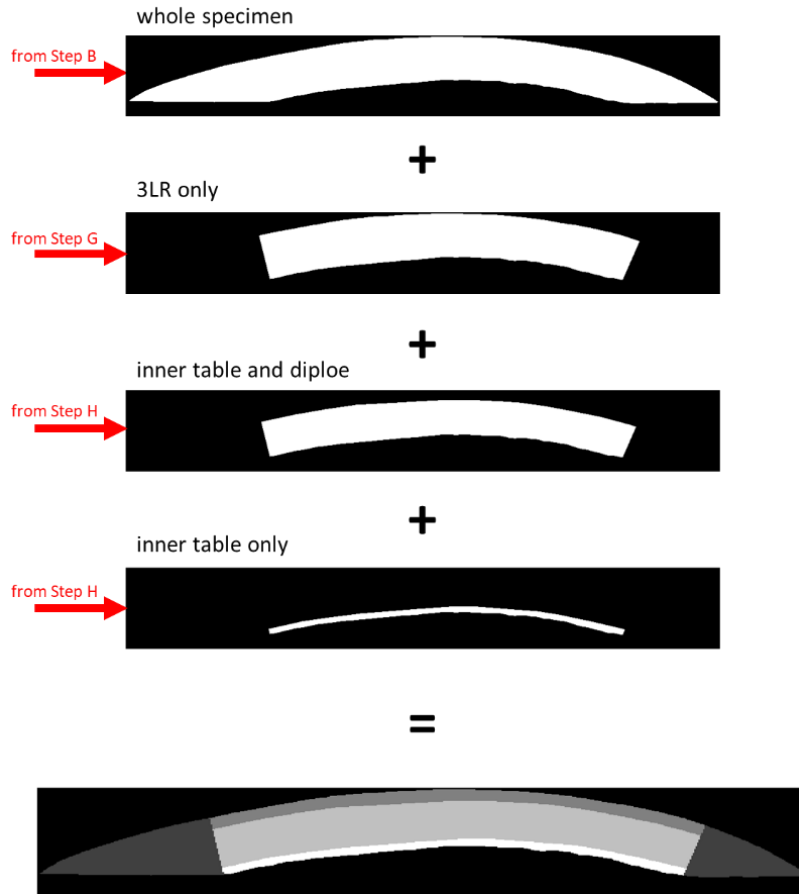


Fig. 5 Creation of the MATLAB Scoring Matrix. Four image-sets from the process outlined in Fig. 3 were loaded into MATLAB and added together. The resulting dataset contained values, which ranged from 0 to 4, as described in Table 1.

Table 1 Physical meaning of the Scoring Matrix values

Physical meaning	Scoring Matrix value
Outside of specimen (air)	0
Composite	1
Outer table	2
Diploe	3
Inner table	4

2.3.3 Comparing Element Location with the Scoring Matrix

The element connectivity and nodal coordinates (as voxel index) were taken from the tetrahedral mesh created in Hypermesh and were imported as matrices into

MATLAB. A MATLAB triangulation object (*triangulation* function) was instantiated from these matrices, to recreate the volumetric mesh within the MATLAB environment. The *incenter* function was used to compute the incenter of each element, which is defined as the center of the inscribed circle of the element. For each element, the value of the Scoring Matrix was queried at the x,y,z coordinates of the element’s incenter. These values corresponded to the block assignment (0 to 4, Table 1) of the element.

Of the 451,070 tetrahedral elements, there were 81 elements for which the scoring method assigned a block of 0. The score of 0 indicated that the element incenter corresponded to a pixel that lay outside of the skullcap, and was therefore an error. This discrepancy was due to the smoothing operations involved in converting the images into an STL and then into a volumetric mesh. To remedy this, the nearest neighbors to these 81 elements were identified with the MATLAB *neighbors* function, and the block assignments of these neighboring elements were queried. The 81 elements were assigned the arithmetic mode of their neighbor’s block assignments.

The results of the element assignment system are shown in Fig. 6.

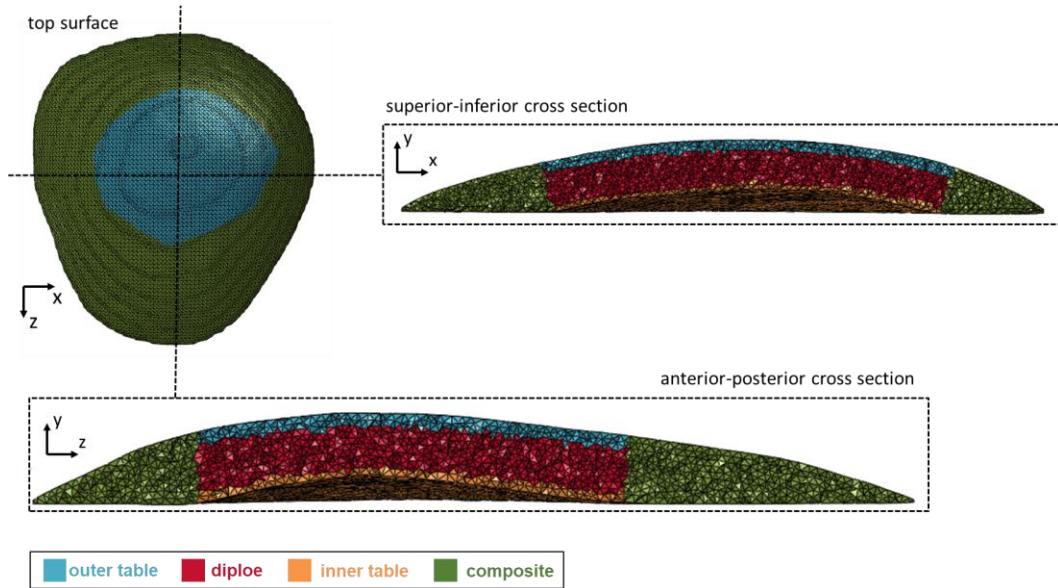


Fig. 6 Volumetric mesh showing the assignment of the different materials

2.3.4 Material Properties

The four materials—composite, outer table, diploe, and inner table—were modeled as linear elastic materials, as shown in Table 2. Their elastic moduli were taken from the results of a previous study by our group (Alexander et al. 2018). In the previous study, the moduli of the three layers of the skull sandwich structure were

computed based on an experimentally-informed model, together with a composite modulus representing a single, homogenized, through-thickness modulus. Different values were calculated for the frontal and parietal bones, accounting for the differences in morphology. The values used here are those that were specific to parietal bones.

The Poisson’s ratio was assumed as 0.3 for each material. The density of each material, ρ , was defined by scaling the density of pure bone (100% bone volume fraction), assumed to be $\rho_0 = 1.8g/cm^3$, by the bone volume fraction (f_{BV}) of the region: $\rho = \rho_0 f_{BV}$. The bone volume fractions for the different regions were taken from the results of a previous study (Alexander et al. 2019) and are reproduced in Table 2.

Table 2 The material properties of the four different element materials. Elastic moduli were taken from the results of ARL-TR-8512 (Alexander et al. 2018). The bone volume fractions were taken from the results of Alexander et al. 2019.

Region	Elastic modulus (GPa)	Poisson’s ratio	Bone volume fraction	Density (g/cm ³)
Composite	2.57	0.3	0.54	0.96
Outer table	7.48	0.3	0.90	1.63
Diploe	1.91	0.3	0.37	0.67
Inner table	6.65	0.3	0.84	1.51

2.4 Finite Element Simulation Setup and Execution

A custom Python script was used to produce an Abaqus input file (.inp) from the volumetric mesh information (Section 2.3), element block assignments (Section 2.3.3), and the material properties of each block (Section 2.3.4). The .inp file produced by this script was then loaded into Abaqus/CAE 6.12, where boundary conditions were specified and the finite element simulation was executed using the direct solver with four processors. Figure 7 provides a high-level flowchart of the process.

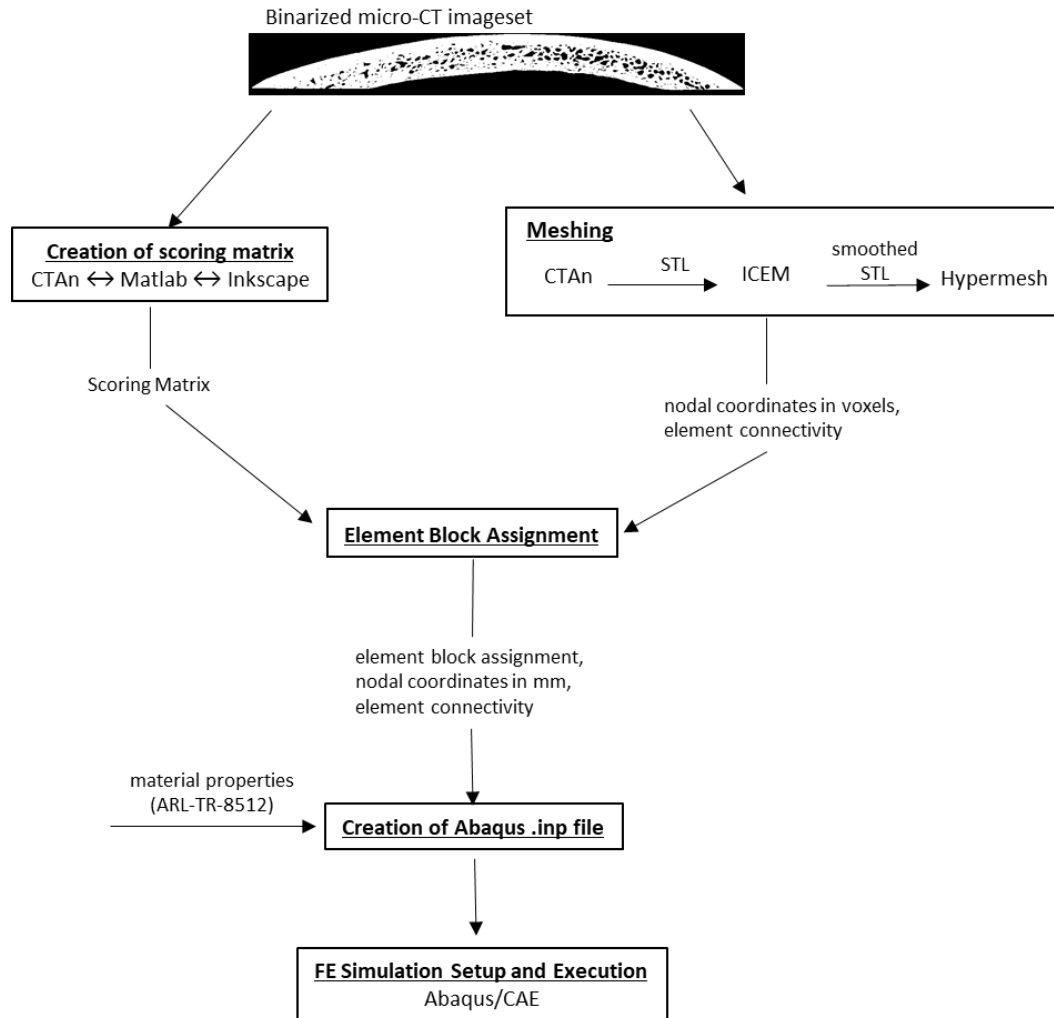


Fig. 7 Steps taken from the micro-CT image-set to the execution of the finite element simulation

2.4.1 Indenter

Figure 8 shows the skullcap specimen and the indenter. The indenter was modeled in Abaqus as a discrete rigid hemisphere of radius 1.25 inches. The position of the indenter in the orthogonal plane was specified to match the POI from the experiment (shown in Fig. 1b). Finally, the y-coordinate was adjusted so that there was a minimal gap (<0.05 mm) between the indenter head and the top of the specimen. The indenter had a zero-displacement boundary condition in the X and Z axis and fixed rotation about all axes. A displacement of 1 mm was specified in the Y axis over a period of 1 ms. This displacement value corresponded with the amount of indenter displacement in the experiment, after which the specimen's load-displacement curve was no longer linear (see Section 3.1).

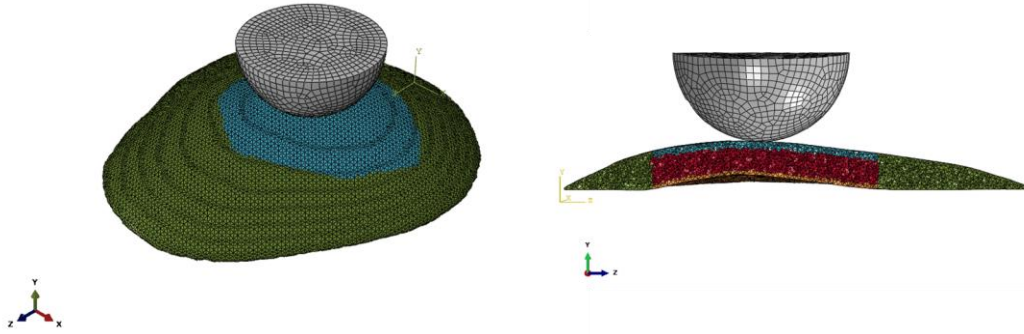


Fig. 8 Skullcap and indenter, viewed from above (left) and from an anterior-posterior cross section (right). The colors within the skullcap mesh indicate the materials of the elements and correspond with those used in Fig. 6.

2.4.2 Backing Plate

The aluminum plate on which the specimen rested during the experiment was also modeled in Abaqus CAE with matching dimensions. The hole in the plate was replicated in the mesh by first finding the x, z coordinates of several points along the perimeter of the bottom surface of the skullcap. A spline was drawn connecting these coordinates on the plate geometry. The resulting curve was then offset by 0.25 inches toward the center of the plate.

During the simulation, the plate was constrained in the x, z, and y directions at eight nodes near the corners of the top and bottom surfaces as shown in Fig. 9. The plate was modeled as aluminum with a modulus of 69 GPa, Poisson's ratio of 0.35, and density of 2.72 kg/cm³.

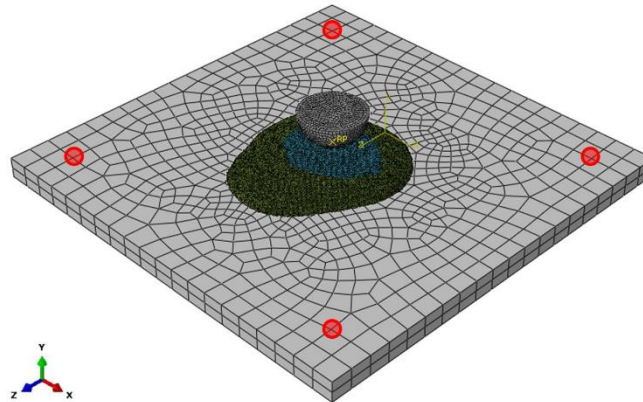


Fig. 9 Assembly of the aluminum backing plate, specimen, and indenter. Four of the nodes used to constrain the plate in the x-z plane are circled in red.

2.4.3 Contact

Contact was modeled using the surface-to-surface formulation of Abaqus/Standard¹, with two contact pairs specified. One pair was between the indenter and the skullcap; this contact was specified to be frictionless. The other pair was between the skullcap and the backing plate, and this contact was specified with a friction coefficient of 0.5. The Abaqus contact formulation also included a zero-penetration constraint between contact pair surfaces. The specimen was constrained in the orthogonal plane (x-z) by constraining the x and z displacements of a set of three nodes nearest to the contact point of the specimen with the indenter.

3. Results

3.1 Indenter Load-Displacement

Figure 10 shows the load during the experiment measured by the load cell connected to the indenter, as a function of indenter displacement measured from the crosshead. The linear portion of the load-displacement curve was identified as approximately occurring between indenter displacement values of 0.40 mm and 0.80 mm. The stiffness in this linear regime was found to be 1.51 kN/mm (dashed black line, Fig. 10).

In the simulation, there was an initial small gap between the indenter and the top surface of the specimen as well as between the bottom surface of the specimen and the backing plate (Section 2.4.1). To compare the simulation with the experimental load-displacement curve, the amount of applied indentation in the simulation was calculated by identifying the first increment for which contact force between the indenter and the specimen was nonzero. The amount of applied indentation will also be referred to as the applied displacement. Figure 10 reports the total contact force from the simulation for the interaction between the indenter and the specimen as a function of the applied displacement. The stiffness of the simulated skullcap was 1.46kN/mm.

¹ Described in Abaqus Analysis User's Guide, Section 36.3.1: Defining contact pairs in Abaqus/Standard

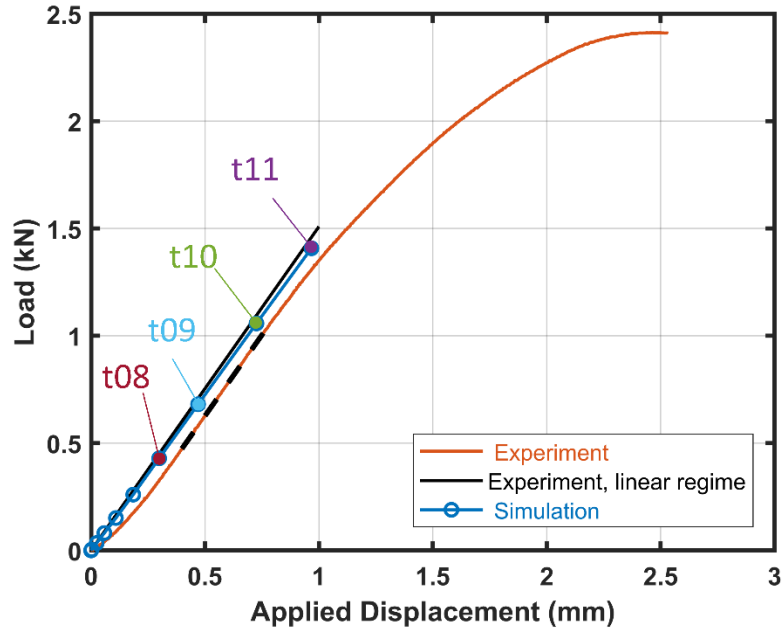


Fig. 10 Load-displacement curve for the indenter, measured during the experiment and simulation. The linear portion of the experimental load-displacement curve is highlighted (black dashed line), and is also replotted from the origin (solid black line). Four timepoints in the simulation that are used for comparison between the simulation and experiment (Section 3.2) are noted by t08-t11.

3.2 Backface Displacement

The displacement in the loading direction (y) from simulation was compared with that of the experiment. It will be referred to as the backface displacement (BD), since it is a direct measure of how much the skull moves toward the brain. Likewise the surface of the skullcap and the surface of the plate facing the cameras will be referred to as the backface. Contours of the BD on the backface of the plate and specimen will be referred to as the full-field BD. The BD was compared for values of applied displacement between 0 and 1 mm and also at the four specific timepoints marked in Fig. 10 as timepoints t08-t11. These timepoints were the last four timepoints in the simulation. For each of the timepoints t08-t11, the corresponding timepoint in the experiment was identified by matching the load between the simulation and experiment. Three different measures of the BD were calculated for comparison: the maximum BD located at a point under the POI (Section 3.2.1), the BD of the plate (Section 3.2.1), and the BD profile (Section 3.2.2).

3.2.1 Maximum Backface Displacement and Plate Displacement

Figure 11 shows the full-field BD for the simulation and the experiment at t11, including both the skullcap and a region of the plate near the skullcap. The full-field BD contours for t08-t10 are included in Appendix A. The maximum BD (BD_{max}) of the skullcap was located at a point on its backface approximately under the POI, and this location is marked in Fig. 11. As the specimen was loaded in the y-direction, it pressed against the backing plate, thus displacing the plate in the loading direction. The resulting BD of the plate is shown in Fig. 11, where the displacement contours of the plate around the specimen have non-zero values. Figure 11 also indicates that the BD of the plate was non-uniform and non-symmetric, due to the plate not being perfectly flat combined with the eccentricity of the loading point relative to the opening in the plate. To aid in comparing the simulation and the experiment, the skullcap displacement was normalized relative to the plate displacement, where the plate displacement was measured as an average of several points along the perimeter of the hole in the plate. Figure 11 shows the location of these Plate Points of Extraction. Figure 12 compares the BD of the Plate Points of Extraction and the BD_{max} of the specimen in order to visualize the magnitude of the skullcap displacement relative to the plate displacement.

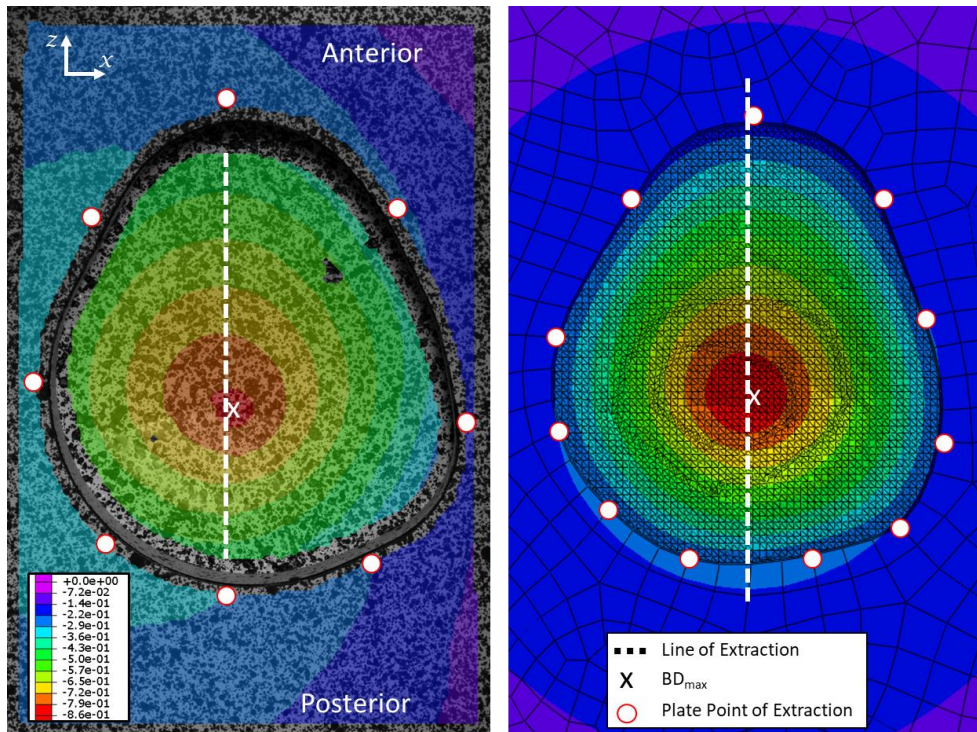


Fig. 11 Contours of the BD for the backface of the skullcap and the plate at the timepoint t11 (timepoints were defined in Fig. 10). The contours from the experiment and simulation are shown on the left and right, respectively. The plate is identified in the simulation by the larger elements, the skullcap by the much smaller elements. Similar contours for t08–t10 are included in Appendix A.

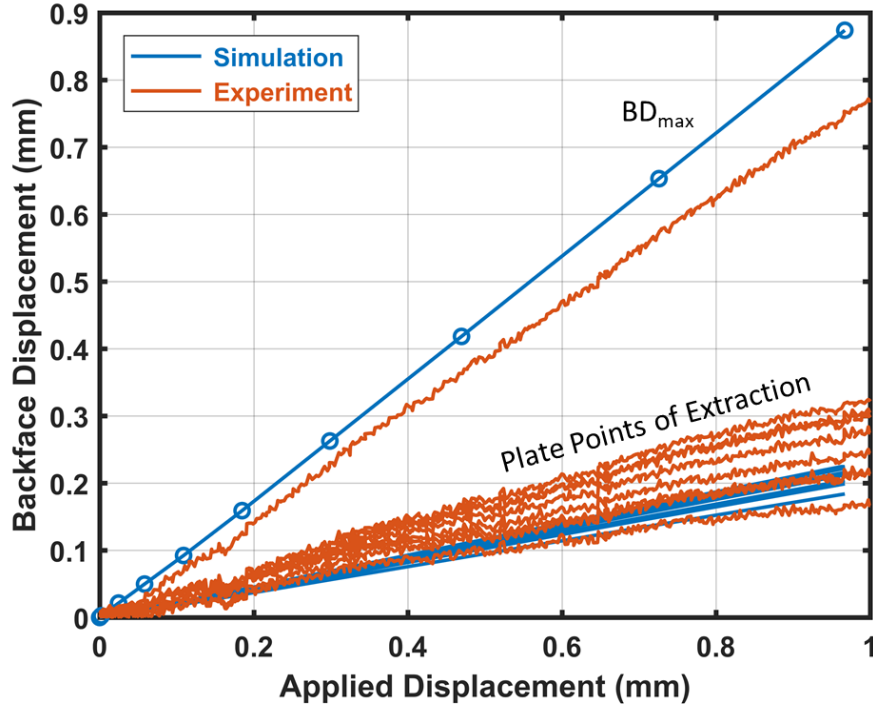


Fig. 12 The maximum BD of the skullcap (BD_{max}), and the BD at several points around the perimeter of the hole in the backing plate (Plate Points of Extraction), are plotted as a function of the displacement applied by the indenter. The location of BD_{max} and the Plate Points of Extraction are shown in Fig. 11.

3.2.2 Relative BD Profile

The BD was also compared between the experiment and simulation for points along a line drawn from the posterior side to the anterior side of the specimen and passing under the POI. This line will be referred to as the Line of Extraction (LoE) and is shown in Fig. 11 as a white dash-line. The BD of the points along the LoE will be referred to as the BD profile. As shown in Fig. 11, the LoE from the experiment was only for the central region of the skullcap exposed to the cameras and therefore did not include the periphery of the skullcap, which was resting on the plate. Moreover, the LoE from the experiment did not extend completely to the plate. The LoE from the simulation extended for the entirety of the skullcap, including the portion resting over the plate.

The BD profile was calculated relative to the plate in order to account for the differences between the simulation and the experiment in the amount of plate displacement. The amount of plate displacement (BD_{plate}) in the experiment was calculated by averaging the values of BD for the experimental Plate Points of Extraction (Fig. 12). The BD_{plate} in the simulation was calculated in an analogous manner, by averaging the values of BD for the Plate Points of Extraction in the simulation. Then, the relative BD profiles for the experiment and simulation were

calculated by subtracting the corresponding BD_{plate} values from the raw BD values. Figure 13 compares the relative BD profiles between the experiment and simulation for the timepoints t08–t11.

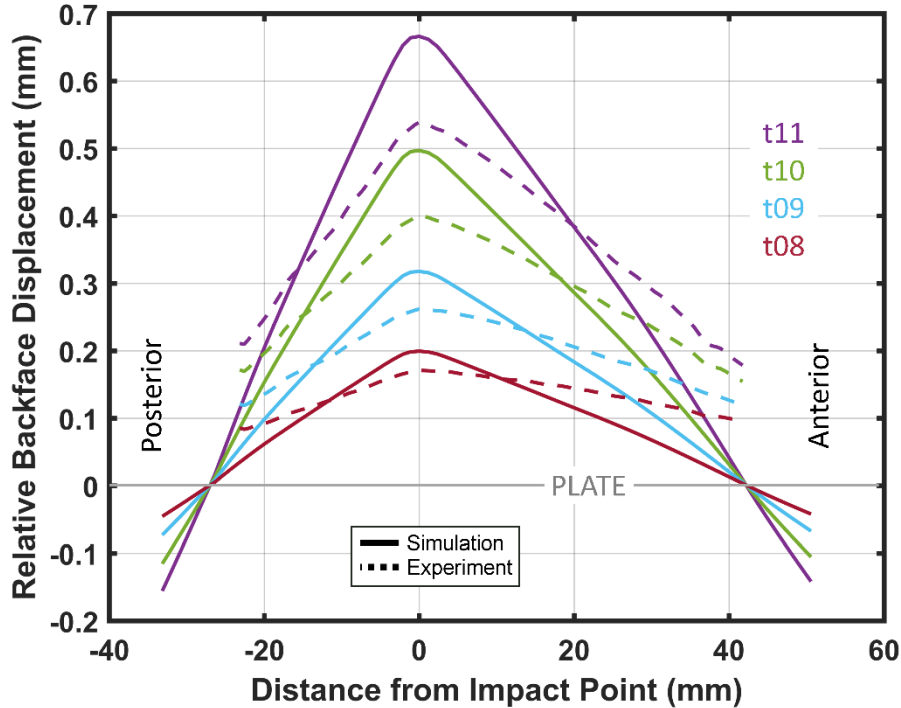


Fig. 13 Relative BD profiles of the skullcap zeroed to the plate for the timepoints t08–t11 (timepoints were defined in Fig. 10). The relative BD is plotted for points along the Lines of Extraction (location shown in Fig. 11). The BD profile is plotted as a function of distance in the z-dimension (Fig. 11) from the point of BD_{max} . The location of BD_{max} was under the POI and is marked as “X” in Fig. 11.

4. Discussion

The load and deformation of the skullcap response to quasi-static indentation was recorded experimentally. The initial linear response was compared to a finite element simulation, which used previously reported mechanical properties of the human skull (Alexander et al. 2018). At roughly 1 mm of indentation applied to the skullcap, the relative BD_{max} in the simulation was 24% higher than in the experiment. The skullcap stiffness in the simulation was 3% lower than the stiffness measured in the linear regime of the experiment.

Many FE simulations involving the head represent the skull as a homogeneous material. The methodology used here was meant to provide an example of how a homogeneous model of the skull could be brought a step closer to biofidelity, by simply remeshing only the impact zone as a three-layer system. To demonstrate the

difference that this remodeling would make in simulations involving head injury, the present indentation simulation was rerun with all elements assigned the properties of the composite (homogeneous) material (Table 2). This simulation will be referred to as the “composite-only FEA” or homogeneous simulation, since the skull was modeled with only a single set of material properties imitating an FE mesh that did not distinguish between the three different skull layers. The load-displacement curve and the relative BD profile at the end of the simulation (timepoint t11) are shown in Fig. 14 and compared to the heterogeneous mesh and the experiment (Table 3). As seen, modeling the three layers of the skull in the impact region significantly improved the ability of the simulation to match the BD and stiffness of the experiment. The BD and stiffness are two metrics of the response of the skull to impact loading, which can be expected to influence head injury outcomes. Therefore, the improved accuracy of the heterogeneous mesh highlights the importance of modeling the skull as a more complex structure in the impact region.

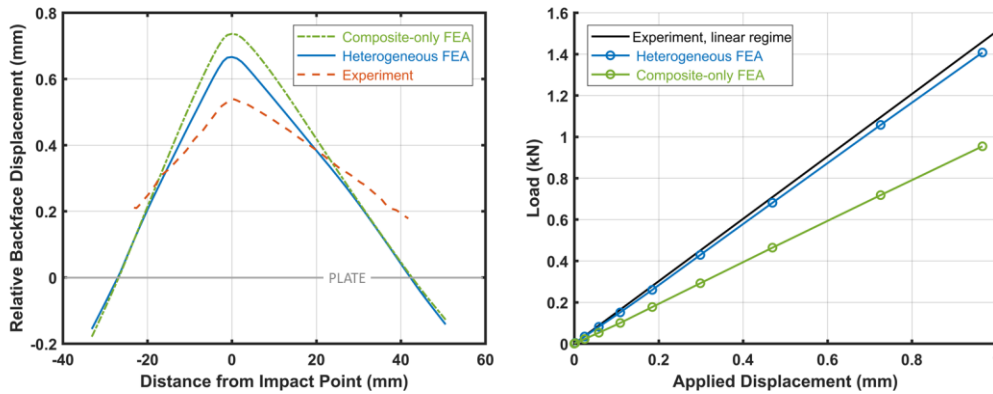


Fig. 14 Relative BD profile at t11 and indentation load when all elements are assigned the same composite mechanical properties (green line). (Left) The BD profile at timepoint t11, relative to the plate. (Right) The load-displacement curves compared to the linear regime of the experiment, which was identified in Fig. 10.

Table 3 Relative BD_{max} at timepoint t11 and the skullcap stiffness. The experimental stiffness is from the linear regime, which was identified in Fig. 10.

	Relative BD_{max} at t11 (mm)	Stiffness (kN/mm)
Experiment	0.54	1.51
Heterogeneous FEA	0.67	1.46
Composite-only FEA	0.74	1.00

Differences between the simulation and experiment are due to the approximations made in modeling the mechanical properties of the skull. First, only three different

sets of material parameters were assigned to the skullcap for the region near the indenter, corresponding to the three layers of outer table, diploe, and inner table. Using only a single material model for each of the layers assumed that the complex mechanical response of each layer could be accounted for by a single model. However, there is potentially a large variation even within a single layer. Using a single model for each layer is an especially drastic approximation for the diploe, since the variation in porosity within this layer has been shown to be substantial (Alexander et al. 2019).

Furthermore, the numerical values of the modulus, density, and thickness for each of the layers also represented an approximation. The variation in thickness, porosity, and mechanical properties between human skulls is well documented. However, the simulation assigned geometric parameters and mechanical properties of the layers from generalized values pooled for different parietal specimens, rather than using values specifically determined for the individual specimen of the present study. These generalized values were used to test their predictive capability when used a priori.

5. Conclusion and Future Work

The initial, linear response of a skullcap specimen, which represented the 3-D curvature of the skull, was successfully modeled by representing the skull as a three-layered structure in the indented region and as a homogeneous material outside of the indented zone. The method was meant to provide an example of how a homogeneous FE model of the skull could be brought one step closer to biofidelity. Thicknesses and moduli were assigned for each layer and for the homogeneous material using averaged values from previous microstructural based experimental studies of the human skull (Alexander et al. 2019, 2020a). The simulation closely matched the linear portion of the experimental response, as indicated by the load-displacement and back surface displacement of the skull. Therefore, the previously published averaged thicknesses and moduli were shown to accurately represent the skull response. Furthermore, the three-layer methodology was shown to provide a closer match to the experimental response compared to modeling the skull as a single, homogeneous material. The same method for heterogeneous material property assignment can be used to apply other material models to each of the different regions (or to each element) in order to successfully model the nonlinear, finite deformation response of the skullcap. Extending the modeling framework to include the nonlinear regime could improve the prediction of fracture patterns in the skull, a fundamental capability in the design and analysis of head protection systems.

6. References

- Alexander SL, Gunnarsson CA, Rafaels K, Weerasooriya T. Microstructural dependence of the compressive mechanical response of human skull. Aberdeen Proving Ground (MD): Army Research Laboratory (US); 2018 Sep. Report No.: ARL-TR-8512.
- Alexander SL, Gunnarsson CA, Weerasooriya T. Structural influence on the mechanical response of adolescent Göttingen porcine cranial bone. Aberdeen Proving Ground (MD): Army Research Laboratory (US); 2016 Oct. Report No.: ARL-TR-7845.
- Alexander SL, Rafaels K, Gunnarsson CA, Weerasooriya T. Structural analysis of the frontal and parietal bones of the human skull. *J Mech Behav Biomed*. 2019 Feb 1;90:689–701.
- Alexander SL, Gunnarsson CA, Rafaels K, Weerasooriya T. Multiscale response of the human skull to quasi-static compression. *J Mech Behav Biomed*. 2020a Feb 1;102.
- Alexander SL, Weerasooriya T. Microstructure-based model of the deformation and failure response of the human skull under uniaxial compression. Aberdeen Proving Ground (MD): CCDC Army Research Laboratory (US); 2020b May. Report No.: ARL-TR-8961.
- Bessho M, Ohnishi I, Matsuyama J, Matsumoto T, Imai K, Nakamura K. Prediction of strength and strain of the proximal femur by a CT-based finite element method. *J Biomech*. 2007;40(8):1745–1753.
- Brown KR, Tarsuslugil S, Wijayathunga VN, Wilcox RK. Comparative finite-element analysis: a single computational modelling method can estimate the mechanical properties of porcine and human vertebrae. *J R Soc Interface*. 2014 Jun 6;11(95):20140186.
- Chen G, Schmutz B, Epari D, Rathnayaka K, Ibrahim S, Schuetz MA, Percy MJ. A new approach for assigning bone material properties from CT images into finite element models. *J Biomech*. 2010 Mar 22;43(5):1011–5.
- Dagro AM, McKee PJ, Kraft RH, Zhang TG, Satapathy SS. A preliminary investigation of traumatically induced axonal injury in a three-dimensional (3-D) finite element model (FEM) of the human head during blast-loading. Aberdeen Proving Ground (MD): Army Research Laboratory (US); 2013. Report No.: ARL-TR-6504.

- Dall'Ara E, Luisier B, Schmidt R, Kainberger F, Zysset P, Pahr D. A nonlinear QCT-based finite element model validation study for the human femur tested in two configurations in vitro. *Bone*. 2013 Jan 1;52(1):27–38.
- Gunnarsson CA, Alexander S, Rafaels K, Walter T, Weerasooriya T. High-rate fracture of human skull. *Mechanics of Biological Systems & Micro-and Nanomechanics*. 2019;4:91–94.
- Helgason B, Perilli E, Schileo E, Taddei F, Brynjólfsson S, Viceconti M. Mathematical relationships between bone density and mechanical properties: a literature review. *Clin Biomech*. 2008;23(2):135–146.
- Morgan EF, Bayraktar HH, Keaveny TM. Trabecular bone modulus density relationships depend on anatomic site. *J Biomech*. 2003;36(7):897–904.
- Otsu N. A threshold selection method from gray-level histograms. *Automatica*. 1975;11(285-296):23–27.
- Thompson KA, Sokolow AC, Ivancik J, Zhang TG, Mermagen WH, Satapathy SS. A sensitivity study of the porcine head subjected to bump impact. In: *ASME 2016 International Mechanical Engineering Congress and Exposition, Volume 3: Biomedical and Biotechnology Engineering*. V003T04A047. American Society of Mechanical Engineers; 2016 Nov 11–17; Phoenix, AZ.
- Zhang TG, Thompson KA, Satapathy SS. Effects of loading conditions and skull fracture on load transfer to head. *ASCE-ASME Journal of Risk and Uncertainty in Engineering Systems, Part B: Mechanical Engineering*. 2018 Jun 1;4(2):021007.

Appendix A. Contours of Fullfield Backface Displacement

The backface displacement (BD) was compared between the experiment and simulation in Section 3.2 of the main report. Figure A-1 compares the fullfield BD contours on the specimen and plate backface (facing the cameras) for the timepoints t08–t11.

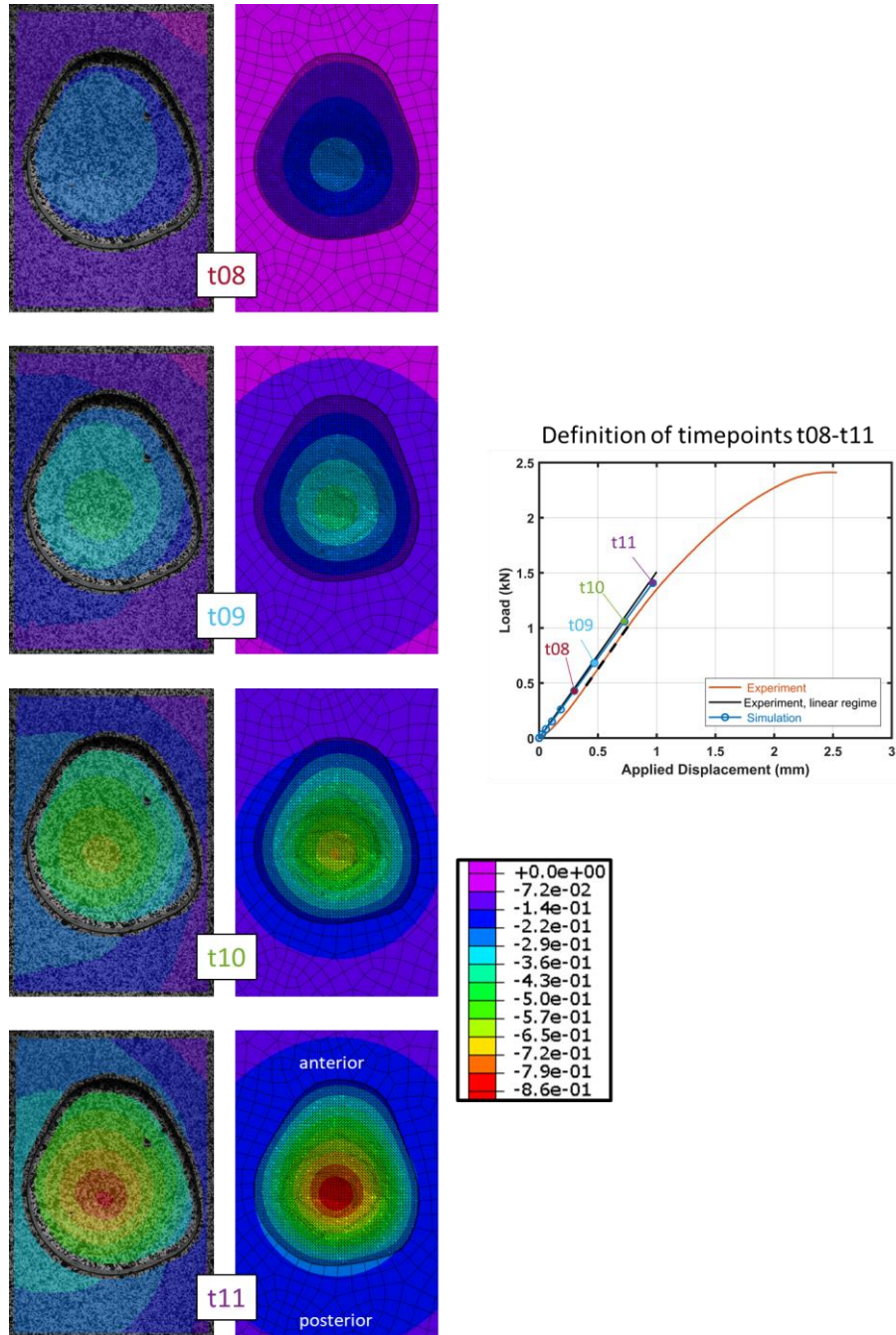


Fig. A-1 Full-field BD contours from the experiment (left column) and simulation (right column) for the timepoints t08–11. The timepoints were previously defined in Fig. 10 of the main report, which is reproduced on the right.

Appendix B. Effect of the Friction Coefficient between Skullcap and Backing Plate

The friction coefficient between the skullcap and the aluminum backing plate was specified as $\mu = 0.50$ in the simulation. This value is in the range for the static frictional coefficient between polymethylmethacrylate (PMMA or Plexiglas) and steel, whether or not the interface is lubricated ($0.4 \leq \mu \leq 0.5$, EngineeringToolbox.com). The effect of friction coefficient was quantified by running the same heterogeneous simulation as presented in Section 2.4 of the main report, while using either a low value ($\mu = 0.25$) or high value ($\mu = 0.75$) for the friction coefficient.

Figure B-1 compares the load-displacement curves using the three different values of coefficients. Table B-1 lists the stiffnesses of these heterogeneous simulations and compares them with the experiment and the composite (homogeneous) simulation, as reported in Table 3. Varying the friction coefficient by 50% to 100% from the original value of $\mu = 0.50$ yielded frictional coefficients that were well outside the range reported for the interface between PMMA and steel. However, even when using these low and high values, the stiffness of the heterogeneous simulation varied by less than 5%, whereas the difference in stiffness between the heterogeneous simulation and the composite (homogeneous) simulation was greater than 30%.

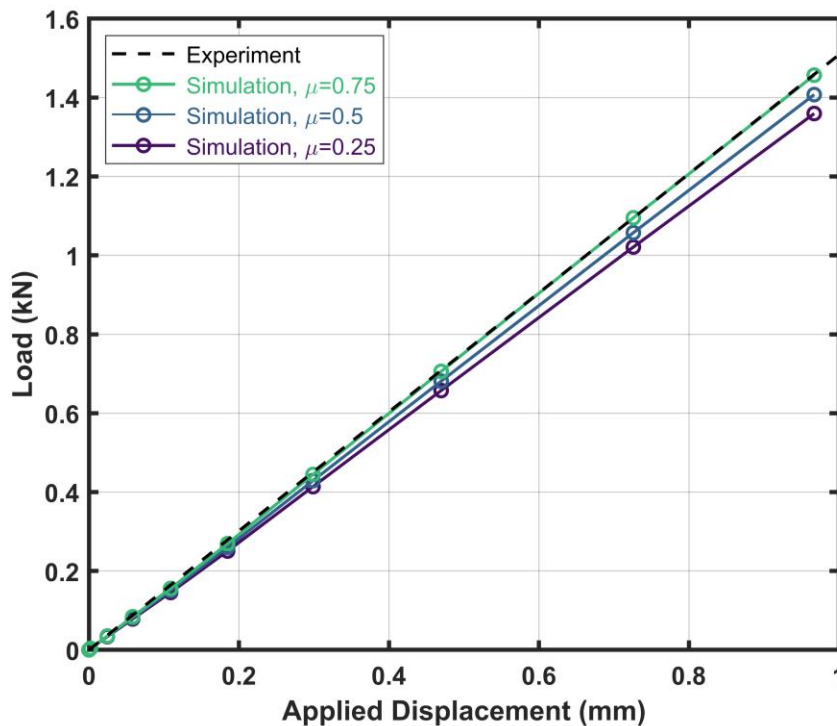


Fig. B-1 Load-displacement response of the heterogeneous simulation using different values of the frictional coefficient between the skullcap and the backing plate. The case of $\mu = 0.5$ (blue curve) corresponds to the heterogeneous simulation presented in Section 3.

Table B-1 Skullcap stiffness

	Stiffness (kN/mm)
Experiment	1.51
Heterogeneous FEA, $\mu=0.75$	1.51
Heterogeneous FEA, $\mu=0.50$	1.46
Heterogeneous FEA, $\mu=0.25$	1.40
Composite-only FEA, $\mu=0.50$	1.00

List of Symbols, Abbreviations, and Acronyms

3-D	3-dimensional
3LR	3-layer region
ARL	Army Research Laboratory
BD	backface displacement
CCDC	US Army Combat Capabilities Development Command
DIC	digital image correlation
FEA	finite element analysis
fps	frame per second
LoE	Line of Extraction
micro-CT	micro-computed tomography
POI	Point of Impact
ROI	region of interest
STL	stereolithography

1 (PDF)	DEFENSE TECHNICAL INFORMATION CTR DTIC OCA	4 (PDF)	MRMC DOD BLAST INJURY RSRCH PROGRAM COOR OFC R GUPTA T PIEHLER R SHOGE F LEBEDA
1 (PDF)	CCDC ARL FCDD RLD CL TECH LIB	2 (PDF)	MRMC JTAPIC PRGM OFC W LEI J USCILOWICZ
1 (PDF)	CCDC ARL ARO FCDD RLR D STEPP	1 (PDF)	WIAMAN PMO K LOFTIS
12 (PDF)	CCDC NATICK SOLDIER SYSTEMS CTR M G CARBONI M CODEGA D COLANTO R DILLALLA B FASEL J FONTECCHIO B KIMBALL J KIREJCZYK J PARKER M MAFEO M MARKEY D PHELPS	4 (PDF)	US ARMY AEROMEDICAL RSRCH LAB F BROZOSKI V CHANCEY B MCENTYRE D WISE
3 (PDF)	PROG EXECUTIVE OFC SOLDIER J HOPPING J MULLENIX D OTTERSON	1 (PDF)	CCDC GROUND VEHICLE SYSTEMS CENTER R SCHERER
1 (PDF)	US ARMY TEST AND EVALUATION COMMAND A FOURNIER	1 (PDF)	CCDC HQ AMSRD PE D RUSIN
1 (PDF)	MTRL SCIENCES DIV LAWRENCE BERKELY NATL LAB R RITCHIE	2 (PDF)	CCDC CHEMICAL BIOLOGICAL CENTER M HORSMON N VINCELLI
5 (PDF)	SOUTHWEST RSRCH INST C ANDERSON JR S CHOCRON D NICOLELLA T HOLMQUIST G JOHNSON	1 (PDF)	OSD DOT&E J IVANCIK
1 (PDF)	NIST M VANLANDINGHAM	5 (PDF)	US NAVAL RESEARCH LABORATORY A BAGCHI A ILIOPOULOS J MICHPOULOS K TEFERRA X TAN
1 (PDF)	INST FOR DEFNS ANLYS Y MACHERET	4 (PDF)	WHITING SCHOOL OF ENGRNG JOHNS HOPKINS UNIV KT RAMESH T D NGUYEN B NOTGHI S BAILOOR

2 (PDF)	COULTER DEPARTMENT OF BIOMEDICAL ENGINEERING GEORGIA INSTITUTE OF TECHNOLOGY S MARGULIES D MCDOWELL	1 (PDF)	UNIVERSITY OF CAMBRIDGE ENGINEERING DEPARTMENT V DESHPANDE
1 (PDF)	DEPT OF ENGRNG SCI AND MECHANICS VIRGINIA POLYTECHNIC INST AND STATE UNIV R BATRA	2 (PDF)	UNIVERSITY OF SOUTH CAROLINA COLLEGE OF ENGINEERING M SUTTON S SOCKALINGAM
3 (PDF)	MASSACHUSETTS INST OF TECHLGY INST FOR SOLDIER NANOTECHNOLOGIES R RADOVITZKY S SOCRATE MJ BUEHLER	4 (PDF)	CCDC DAC FCDD DAS LBW G DIETRICH FCDD DAS LBE J GURGANUS W MERMAGEN S SNEAD
1 (PDF)	DEPT OF MECHL AND NUCLEAR ENGRNG THE PENNSYLVANIA STATE UNIV R KRAFT	84 (PDF)	CCDC ARL FCDD RLD P S WALSH FCDD RLW S KARNA A RAWLETT S SCHOENFELD J ZABINSKI FCDD RLW P R FRANCAERT FCDD RLW L T V SHEPPARD FCDD RLW M E CHIN FCDD RLW B R BECKER J CAMPBELL P GILLICH C HOPPEL B SCHUSTER A TONGE L VARGAS-GONZALEZ FCDD RLW LF T G BROWN FCDD RLW LH A DAGRO T EHLERS C GOOD L MAGNESS C MEYER J NEWILL D SCHEFFLER FCDD RLW MA T BOGETTI D O'BRIEN T PLAISTED J SANDS E WETZEL
1 (PDF)	INDIAN INST OF TECH R BHARDWAJ		
2 (PDF)	CENTER FOR APPLIED BIOMECHANICS UNIVERSITY OF VIRGINIA R SALZAR MB PANZER		
1 (PDF)	UCSD MATERIAL SCIENCE AND ENGINEERING MARC MEYERS		
1 (PDF)	DUKE UNIVERSITY BIOMEDICAL ENGINEERING CR BASS		
1 (PDF)	UNIVERSITY OF CAPE TOWN BLAST IMPACT & SURVIVABILITY UNIT TJ CLOETE		
1 (PDF)	UNIVERSITY OF OXFORD BLAST IMPACT & SURVIVABILITY UNIT C SIVIOUR		

C YEN
FCDD RLW MB
G GAZONAS
B LOVE
P MOY
J SIETINS
J SUN
T WALTER
FCDD RLW MC
A BUJANDA
R JENSEN
J LA SCALA
FCDD RLW MD
B CHEESEMAN
K CHO
FCDD RLW ME
J LASALVIA
P PATEL
S SILTON
J SWAB
FCDD RLW MF
K DARLING
B DOWDING
S GREндаHL
H MURDOCH
FCDD RLW MG
J ANDZELM
J LENHART
K MASSER
R MROZEK
FCDD RLW PA
S BILYK
FCDD RLW PB
S ALEXANDER
T BAUMER
A BROWN
B FAGAN
A GOERTZ
A GUNNARSSON
C HAMPTON
M KLEINBERGER
E MATHEIS
J MCDONALD
P MCKEE
K RAFAELS
S SATAPATHY
M TEGTMEYER
T WEERASOORIYA
S WOZNIAK
T ZHANG
FCDD RLW PC
J CAZAMIAS
D CASEM
J CLAYTON
C MEREDITH
L SHANNAHAN

J LLOYD
A TONGE
FCDD RLW PD
R DONEY
C RANDOW
FCDD RLW PE
M LOVE
P SWOBODA
FCDD RLW PF
N GNIAZDOWSKI
R GUPTA
S KUKUCK